Defect complexes in Li-doped MgO

N. A. Richter,[1] F. Stavale,[1] S. V. Levchenko*,[1] N. Nilius*,[1,2] H.-J. Freund,[1] and M. Scheffler[1]

[1] *Fritz-Haber-Institut der Max-Planck-Gesellschaft, Faradayweg 4-6, 14195 Berlin, Germany*
[2] *Carl von Ossietzky Universität Oldenburg, Institut für Physik, D-26111 Oldenburg, Germany*

Magnesium oxide (MgO) is used in a variety of industrial applications due to its low cost and structural stability. In heterogeneous catalysis, MgO and Li-doped MgO have been studied as catalysts for the oxidative coupling of methane. In this work, we analyze the structure and stability of defect complexes comprising Li dopants and oxygen vacancies in MgO, combining scanning tunnelling microscopy, photon-emission experiments, and density-functional theory computations. The experimental results strongly indicate that after annealing Li-doped MgO to temperatures of 600 K and higher, Li evaporates from the surface, but Li defects, such as substitutional defects, interstitials, or defect complexes comprising Li remain in the bulk. Our calculations show that bulk defect complexes containing F^{2+} color centers, that have donated their two electrons to two adjacent Li defects, are the most stable configurations at realistic pressure and temperature conditions.

PACS numbers: 68.55Ln, 61.72.J-, 68.37.Ef, 61.72Bb

I. INTRODUCTION/MOTIVATION

Introduction – MgO has been studied extensively as a catalytically active material and as a catalyst support. Its functionality as a catalyst can be enhanced when its electronic and morphological properties are modified in a suitable manner, e.g. by defects or dopants. A prominent example in this regard is Li-doping of MgO, which was employed to improve the performance of MgO as a catalyst for the oxidative coupling of methane. It was suggested by Ito and Lunsford in 1985 that in Li-MgO, activated surface oxygen species are produced by substituting divalent Mg with monovalent Li ions, generating electron-holes in the oxygen electronic bands. It was further assumed that electron transfer from methane into these low-lying hole-states triggered the abstraction of an H-atom from the adsorbate as the initial step for subsequent coupling reactions of the remaining CH_3 units to longer hydrocarbons[1]. Although put forward long ago, this mechanism for the oxidative coupling of methane still poses a number of questions, both from the experimental and theoretical viewpoint[2–4]. Based on a review of experimental and theoretical studies, Arndt *et al.* demonstrated that the suggested reaction pathway cannot be a dominating one[3]. In fact, the role of Li is not yet understood. Li substitutional defects in MgO lead to shallow acceptor levels (hole-states) close to the valence band maximum that is mainly composed of O 2 p states. However, the holes may be quickly filled with electrons from adjacent O vacancies that are potential electron sources and act as compensating defects for the Li dopants. As a consequence, the formation of neutral or charged defect complexes containing one or two Li atoms adjacent to an O vacancy can be favorable. On the other hand, Li interstitials can also serve as electron donors - a possibility that has not been explored so far . Our objective is to understand what type of lithium-mediated defect complexes can be present under equilibrium conditions, and to analyse their electronic and structural properties. A combination of scanning tunnelling microscopy (STM), optical spectroscopy and electronic-structure calculations using density-functional theory (DFT) has been used to investigate point-defect complexes in Li-doped MgO. Whereas STM and cathodo-luminescence spectra revealed experimental signatures for the Li-induced defect complexes, the calculations provided information on their formation energies and thermodynamic stabilities, calculated as a function of temperature, Fermi energy, and Li chemical potential. In our photon-emission experiment, we observe a red-shift of the fundamental MgO photon-emission peak upon doping, indicating new electronic states in the band gap. As mentioned above, O vacancies in MgO generally produce such gap states, however neither the precise configuration nor the charge state of relevant defect complexes is known *a priori*.

In order to reproduce the experimental situation, we have explored a variety of defect configurations, using the *ab initio* atomistic thermodynamics approach[5]. For charged defects, also the position of the Fermi level ϵ_F has been taken into account. In addition to the formation energies, the total and atom-projected densities of states were analysed for low-energy defects. On this basis, gap states were identified that are potentially relevant for the new electron-hole recombination channels observed in experiment.

II. METHODOLOGY

Experimental methods – STM experiments were performed in an ultrahigh vacuum environment at liquid nitrogen temperature. Electron tunneling through the MgO band gap was possible only for film thicknesses below 5 ML. Accordingly, atomic resolution could be achieved only in this thickness range. For thicker films (up to 50 ML) relevant for doping, electron hopping was identified as the dominant transport mechanism for electrons through the dielectric layer[6]. Our setup is equipped with an optical readout that enables the collection of photons from the tip-sample junction and their detec-

tion with a charge-coupled device unit outside the vacuum chamber. By this means, spatially resolved optical measurements have been carried out in a wavelength window of 200-1200 nm, using the STM tip as local electron source. The photons are generated by radiative recombination of excitons created by electron injection. Electrons with 100-150 eV energy and 5 nA current were injected into flat and well-ordered oxide regions that have been selected via STM topographic imaging prior to any optical measurement. The spatial resolution of our optical experiments is of the order of 150×150 nm^2 at the given excitation bias. Lower electron energies did not result in a measurable emission response of the oxide film, in contrast to conventional metal surfaces where intense plasmon-mediated light can be detected already at 5 V sample bias. Note that the impact of energetic electrons causes the MgO surface to degrade with time due to electron-stimulated O desorption[7]. We have tried to minimize this effect by choosing fresh sample areas for every experimental run and by keeping accumulation times for spectral acquisition below 60 s.

The MgO films used in the experiments were grown by reactive deposition of Mg in 5×10^{-10} atm O_2 onto a sputtered and annealed Mo(001) single crystal[8]. The oxide has been crystallized via annealing to 1000 K, producing a sharp square pattern in low-energy electron diffraction (Fig. 1 (a), left inset). STM measurements revealed an atomically flat oxide surface, exposing a network of mainly [100]-oriented dislocation lines (Fig. 1 (a), right inset)[8]. The line defects develop spontaneously in the film in order to compensate for the 5.4 % lattice mismatch with the Mo(001) surface beneath[9].

Lithium-doped MgO samples of 15 ML thickness were prepared in two different ways: embedding lithium into the bulk lattice by magnesium and lithium codeposition onto the Mo(001) surface in oxygen, or post-deposition of Li onto the as-grown MgO film followed by an annealing step. The initial concentration of Li in the films was set to about 10 at% (one Li atom per 10 Mg atoms). However, we expect that a considerable part of Li is lost during annealing. The final concentration of Li could not be determined in our experiments.

DFT calculations – To identify possible defect complex configurations, their formation energies are calculated using DFT. For bulk defect complexes, simple-cubic MgO supercell models including 64, 216, and 512 atoms are used. We also considered selected surface defect complexes (see below). The formation energy $G_\mathrm{f}(T,p)$ for each defect configuration is calculated as follows:

$$G_\mathrm{f}(T,p) = E_\mathrm{def} - E_\mathrm{host} + \sum_i n_i\mu_i(T,p_i) + q\epsilon_\mathrm{F} + \sum_i p_i\Delta\mathrm{V} + \Delta F_\mathrm{vib}(T). \quad (1)$$

Here, n_i denotes the number of atoms of species i that have been removed from ($n_i > 0$) and/or added to ($n_i < 0$) the pristine system. E_def and E_host are the DFT total energies of the system with and without the defect. The chemical potential of species i, $\mu_i = \mu_i^\mathrm{ref} + \Delta\mu_i(T,p_i)$ is referenced to μ_i^ref. For O we compute the chemical potential with respect to the total energy of an isolated O_2 molecule. The experimental binding energy without zero-point energies for an O_2 dimer is -5.22 eV[10], while the calculated value is -6.23 eV at PBE[11] level and -5.32 eV when HSE06[12,13] is used. We correct the DFT error in the O_2 binding energy by using the experimental value[14]. The temperature and pressure dependence enters $\Delta\mu_\mathrm{O}(T,p_{\mathrm{O}_2})$ as

$$\Delta\mu_\mathrm{O}(T,p_{\mathrm{O}_2}) = \Delta\mu_\mathrm{O}(T,p^0_{\mathrm{O}_2}) + \frac{1}{2}\mathrm{k}T\ln(\frac{p_{\mathrm{O}_2}}{p^0_{\mathrm{O}_2}}), \quad (2)$$

where $\Delta\mu_\mathrm{O}(T,p^0_{\mathrm{O}_2})$ at $p^0_{\mathrm{O}_2}$=1 atm is obtained from thermochemical tables. We calculate formation energies for a temperature of 600 K and an O_2 partial pressure of 10^{-10} atm ($\Delta\mu_\mathrm{O}(600\ \mathrm{K}, 10^{-10}\ \mathrm{atm}) = -1.21$ eV), as a set of characteristic conditions for the experiment.

The chemical potential of Mg is deduced from the condition of thermodynamic stability of bulk MgO:

$$\mu_\mathrm{Mg} + \mu_\mathrm{O} = E^\mathrm{bulk}_\mathrm{MgO}, \quad (3)$$

where the DFT total energy of an MgO unit cell $E^\mathrm{bulk}_\mathrm{MgO}$ approximates the corresponding Gibbs free energy. For Li, we consider different chemical potentials ranging between the free energy of the Li atom and that of Li in Li_2O. Since the concentration and chemical potential of Li are unknown, we focus on small defect concentrations, when the interaction between defect complexes and the change in volume ΔV of the crystal due to doping can be neglected. This approach significantly simplifies the problem, but still describes the physically meaningful limit.

The contribution of phonons to the formation energy has been calculated for 3×3×3 MgO supercells (216 atoms), using the finite displacement method as implemented in Phonopy[15]. For the most stable defect complexes, the vibrational energy contribution to the defect formation energy is <0.14 eV (calculated with the

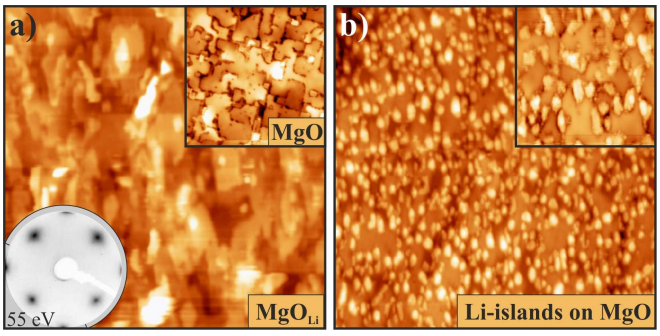

FIG. 1. STM topographic images of (a) a 15 ML thick MgO_{Li} mixed film on Mo(001) and (b) a pristine 15 ML thick MgO film after exposure to 0.2 ML Li (200×200 nm^2). The insets display bare MgO (a) and the corresponding LEED pattern measured at 55 eV electron energy, and a close up of a Li-covered film (b). Both insets are 50×50 nm^2 in size. (V_s = 3.5 V)

PBE functional) in the temperature range below 1300 K (Fig. 2). The vibrational free energy does not have an

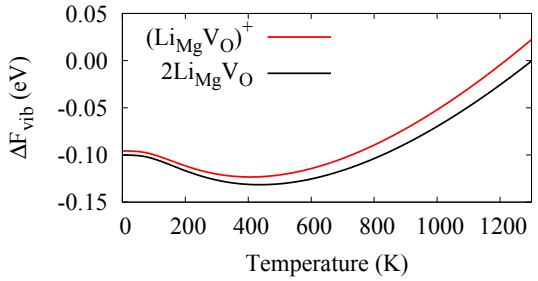

FIG. 2. Vibrational free energy contribution $\Delta F_{\rm vib}$ to the formation energy $G_{\rm f}(T,p)$ for two defect complexes as a function of temperature, calculated using the PBE functional for 216-atom supercells. $\Delta F_{\rm vib}(T)$ is the difference between the vibrational free energy for the MgO system with a defect complex and the vibrational free energy for the pure MgO host system.

effect on the energy hierarchy of the defect complexes considered here. In the formation energies reported below, the vibrational contribution is therefore omitted.

The FHI-aims electronic structure package[16] is employed for all DFT calculations. The numerical settings are the *tight* predefined settings. This approximately corresponds to a double-zeta polarized Gaussian basis set with additional polarization and diffuse functions[16].

For *neutral* defect configurations, convergence tests for increasing cell sizes with fully relaxed coordinates show that interactions between the defect and its periodic images vanish fast with increasing supercell size. The formation energies of these defect complexes are already converged within 50 meV for cubic supercells of 64 atoms (cell length 8.435 Å). To remove spurious electrostatic interactions for *charged* defects, the formation energies are extrapolated to the limit of isolated, non-interacting defects by calculating $G_{\rm f}(L)$ for 64-, 216-, and 512-atom cubic supercells (with L=8.517 Å, L=12.775 Å and L=17.034 Å, respectively) and fitting it to

$$G_{\rm f}(L) = G_{\rm f} + a_1 L^{-1} + a_3 L^{-3}, \qquad (4)$$

where $G_{\rm f} = G_{\rm f}(L \to \infty)$ is the formation energy of the defect at low concentration. We prefer the extrapolation procedure over finite size correction schemes, because it accounts for geometric relaxation effects[17–19]. Fully relaxed coordinates for all systems are calculated using the PBE exchange-correlation functional at the respective optimized lattice parameter (4.258 Å). The relaxed geometries for the 2×2×2 MgO supercell are then scaled to the HSE06 optimized lattice parameter (4.218 Åversus experimental 4.207 at T = 20 K[20]) and a HSE06 single-point calculation is performed for the scaled, relaxed structures. For the extrapolation, we find that coefficients a_1 and a_3 obtained from PBE and HSE06 are very close. Therefore, we determine these coefficients with PBE and use them to extrapolate the formation energy of an isolated defect configuration from the HSE06 calculation of the 2×2×2 supercell. For the smallest (64-atom) bulk unit cell, we used a 4×4×4 k-point mesh, and down-scaled it accordingly for larger unit cell sizes. For the surface defects, defect complexes at the corner of a 2 layer 3×3 atom MgO island on a 4 layer MgO (100) surface slab with a vacuum layer thickness of 100 Å between repeated slabs were calculated using a 4×4×1 k-point mesh. The employed basis set and k-point settings are converged for both PBE and HSE06 calculations.

For three defect structures, $(Li_{Mg}V_O)^+$, $2Li_{Mg}V_O$, and Li_{Mg} (shown in Fig. 7 and discussed in detail below), relaxed atomic coordinates have also been calculated with HSE06. The error in defect formation energy, made by using the PBE relaxed, scaled to HSE06 lattice constant geometries, was found to be < 0.03 eV, and the HSE06 relaxed geometries are practically equivalent to those relaxed with PBE. This is in particular interesting for the Li substitutional defect, where symmetry breaking has been predicted by Lichanot *et al.* in an unrestricted Hartree-Fock study[21]. Using the Hartree-Fock (HF) method leads to localization of the Li valence electron on one nearest-neighbor O atom and as a consequence the distance between the Li atom and this O atom is elongated with respect to the equilibrium MgO bulk interatomic distance. Indication (but no rigorous proof) for this has also been found in electron paramagnetic resonance spectroscopy (EPR) and electron nuclear double resonance spectroscopy (ENDOR) experiments by Abraham *et al.*[22,23]. In the present work, three different starting geometries have been tested for the HSE06 geometry relaxation: (i) the relaxed symmetric PBE structure, (ii) a structure where the Li atom has approached one of its nearest-neighbor O atoms, according to the equilibrium structure found in Ref.[21] using HF, and (iii) a structure where the Li atom is slightly displaced in all three dimensions. In all three cases, calculating the relaxed atomic coordinates using HSE06 resulted in a symmetric structure, as the one obtained with PBE. The total energy difference between the system with starting geometry (ii) and the system with relaxed coordinates, calculated using the HSE06 functional, is < 0.1 eV.

III. RESULTS AND DISCUSSION

A. Experimental results

MgO films with small Li amounts incorporated into the bulk layers still exhibit the rocksalt lattice of the bare oxide[2]. However, the film crystallinity is reduced, i.e., oxide terraces are smaller and defect lines are less straight than in the non-doped case (Fig. 1 (a)). We relate the lower film quality to a mixture of kinetic and thermodynamic effects. First, Li-doped films cannot be annealed as thoroughly as pristine ones, as the alkali impurities tend to leave the oxide at temperatures beyond 800 K. And second, the presence of Li perturbs the crystalliza-

tion process of the rocksalt lattice, e.g., by enriching in the dislocation lines, occupying interstitial lattice sites and agglomerating into tiny Li-O units.

Ad-lithium deposited at 300 K, on the other hand, grows into monolayer islands on the surface (Fig. 1 (b)), as discussed in earlier work[2,24]. The formation of 2D islands is not so much the consequence of strong Li-MgO interface interactions, but results from a considerable barrier for Li up-step diffusion that impedes the development of 3D particles[25]. Upon annealing above 600 K, the Li ad-structures quickly disappear from the surface. While the majority of Li simply evaporates into the gas-phase as Li_2O, a small amount diffuses into the film, as demonstrated below.

The Fermi level of thin MgO films is largely controlled by the metallic Mo support. For films below 5 ML thickness, it can be measured by tunneling spectroscopy. In pristine MgO, the onsets of valence (VB) and conduction band (CB) have been determined to be Δ_{VB}=-5.0 eV and Δ_{CB}=+2.5 eV, respectively. Li doping introduces empty states near the top of the VB, hence well below the Fermi level of the Mo support. As a result, the Li-induced hole states fill up spontaneously via electron transfer from the metal support, causing the oxide film to charge up negatively with respect to the metal. The dielectric film responds to this charge transfer with an upshift of both, VB and CB, which implies a movement of the Fermi level towards the valence band maximum (VBM), as discussed in Ref.[26]. The band shift $\Delta\phi$ is limited by the initial onset of the VB for the pristine film, $\Delta\phi_{max} = -\Delta_{VB}$. Obviously, the width of the space charge layer cannot exceed the film thickness d. Furthermore, it cannot exceed a certain value d_{max} due to the limitation on $\Delta\phi_{max}$. Assuming a constant doping profile with concentration N (number of Li atoms per unit volume), the width of the space charge layer within the slab is limited by

$$d_{max} = \sqrt{\frac{2\epsilon_0\epsilon\Delta_{VB}}{e^2N}}, \tag{5}$$

where ϵ_0 is the vacuum permittivity and ϵ is the static dielectric constant of MgO ($\epsilon = 9.34$[27]). The band shift $\Delta\phi$ can be estimated to:

$$\Delta\phi = \begin{cases} -\frac{e^2N}{2\epsilon_0\epsilon}d^2, & d \le d_{max} \\ -\Delta_{VB} & d > d_{max} \end{cases} \tag{6}$$

Given the loss of Li during film annealing, the actual Li concentration in the films is likely lower than the initial 10 at%. For a 15 ML MgO film (31.5 Å) with a doping concentration of 0.8 at% (eight out of thousand Mg atoms replaced by Li), the downshift of the Fermi level is calculated to 4 eV. For Li concentrations $\geq$ 0.8 at% we therefore expect the Fermi level position to be between 1 eV above the VBM and the Fermi level in the bulk doped oxide, which is close to the VBM.

In both preparations, Li embedding into the bulk lattice and annealing of Li islands, the formation of Li defects in the MgO becomes manifest from distinct changes

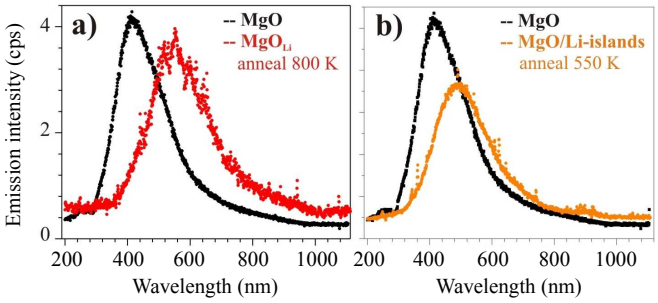

FIG. 3. Cathodo-luminescence spectra of (a) bare and mixed MgO_{Li} films of 15 ML thickness and (b) bare and Li-covered MgO films of 15 ML thickness after annealing to 550 K. All spectra were taken with V_s = 150 V, I = 1 nA and 60s accumulation time. Note the pronounced red-shift of the main emission peak when Li is present in the MgO lattice.

in the optical response of the oxide film (Fig. 3). Pristine MgO films of 15-100 ML thickness display a characteristic 400 nm emission peak in cathodo-luminescence spectroscopy performed in our STM setup[8]. We have assigned this peak to the radiative recombination of electron-hole pairs excited by the incoming electrons across the band gap[28]. These excitonic modes are mobile in the bulk lattice but get trapped at low-coordinated surface sites, in particular at O corner and kink sites, where recombination takes place in a second step[29,30]. The 400 nm emission peak is therefore representative for exciton recombination at low-coordinated surface sites and can be quenched by dosing small amounts of metals, e.g. gold, onto the oxide film[31].

The characteristic optical signature of the pristine film changes significantly upon Li incorporation. Most importantly, the emission maximum in the spectrum undergoes a wavelength shift by 100-150 nm and now peaks at around 550 nm (Fig. 3 (a,b)). These spectral trends have also been observed for films of up to 100 ML thickness. The red-shift suggests the development of new recombination channels for the excitonic modes in the presence of Li defects, for instance via new localized states in the MgO band gap. This implies that the bulk excitons get trapped and recombine already in deeper layers of the film. We discard the possibility that the Li-induced gap states are surface states, as the new optical signature and hence the new recombination channel is insensitive against adsorption of rest gas molecules, such as water, CO or hydrogen. In addition, surface O defects can quickly disappear at the experimental conditions via heterolytic water splitting and formation of OH groups, as discussed below. We hence suggest that the low-energy emission signature observed on Li-doped MgO films relates to the presence of Li-induced defect complexes in the volume of the film. To corroborate this assumption we have calculated the thermodynamic stability and electronic properties of several possible MgO defects developing in presence of Li in the lattice.

B. Theoretical results

1. Bulk and surface defect complexes

The electronic structure of F centers in MgO is characterized by a defect level deep in the band gap, which is occupied by 2 electrons in the neutral F^0 center, by 1 electron in the F^+ center, and which is empty in the F^{2+} center[32]. Li dopants introduce empty states close to the VBM (*p*-type doping), which enables the electrons from the F^0 and F^+ center to lower their energy by jumping into the hole states. An F^0 vacancy adjacent to a Li substitutional defect can transfer one electron to O ions surrounding the Li ion, and turn into an F^+ defect, building a defect complex together with the Li ion. In analogy, an F^0 vacancy adjacent to two Li substitutional defects evolves to an F^{2+} defect upon electron transfer, within a defect complex that comprises two Li atoms and an O vacancy. The short distance for the charge transfer ensures low energy cost of the charge separation. Local geometric and electronic relaxation, which obviously strongly depends on the atomic configuration, can further lower the formation energy of the defect complex.

The frequency shift that is observed in the cathodoluminescence spectra, when comparing pure MgO to MgO with Li, shows that the preferred decay channel for excitons created in the experiment changes, when Li is present in the sample. As mentioned above, defect complex formation comprising Li dopants and O vacancies can provide electronic levels in the gap that can open a new exciton decay channel, where electron-hole pairs excited in the cathodo-luminescence experiment can recombine via a defect level in the band gap. However, the defect level must be half-filled or empty, so that an excited electron in the conduction band can lower its energy to the defect level and finally to the electron reservoir ϵ_F at the valence band maximum. This means, that defect complexes comprising F^+ or F^{2+} centers are possible candidates to explain the observed photon-emission response. In contrast, neutral or charged Li defect configurations without O vacancy, like Li substitutional defects, interstitials or a combination of both, cannot open new decay channels, since they do not exhibit defect states in the gap. However, in the theoretical analysis also these defects are considered. Note, that an emission peak due to direct electron-hole pair recombination across the bulk MgO band gap would appear outside the spectral window that was accessible in the experiment.

In the following, we will use a simplified Kröger-Vink notation that suppresses the electronic charge of the species relative to the original site. A defect $(M_S)^q$ describes a species M (for instance M=Li) or a vacancy (M=V) occupying the site of species S (S=Mg, S=O, or S=i for an interstitial). The charge state of the defect, in case of an extra or a removed electron, is specified by q.

Li is expected to leave the surface in the form of Li_2O molecules at temperatures above 800 K. However, at lower temperatures defect complexes comprising one or two Li ions and F^+- or F^{2+} centers can be formed both at the surface and in the bulk. In fact, we find that the free formation energy of all considered defects is lower at the surface in a wide range of conditions in the absence of water. However, in reality water is always present in the experiment, and can interact with defects at the surface. To test this scenario, we estimate the stability of a defect complex comprising an F^{2+} vacancy adjacent to two Li substitutional defects $2Li_{Mg}V_O$ at the corner of a 2 layer 3×3 atom MgO island on a 4 layer MgO (100) surface slab (Fig. 4 (a)). The formation energy of this defect

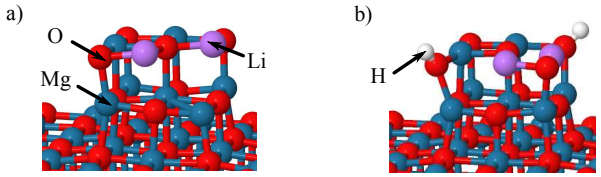

FIG. 4. Models for calculating the stability of a defect complex comprising an F^{2+}-type O vacancy adjacent to two Li substitutional defects at the corner. (a) $2Li_{Mg}V_O$ corner defect complex. (b) Hydrogenatively annihilated defect complex $2Li_{Mg}2H$.

complex is compared to the formation energy of a configuration $2Li_{Mg}2H$ after hydrogenative annihilation, where two hydrogen atoms of a water molecule have formed OH groups with the surface O atoms nearby the Li dopants, while the O atom has "healed" the vacancy (Fig. 4(b)). The difference in free formation energy between the two systems is in favor of vacancy healing for temperatures of 600 K and below and water pressures of 10^{-14} atm and above (Fig. 5). In principle, vacancy healing is also possible for bulk defect complexes in the presence of water due to the diffusion of hydrogen or OH into the bulk (not considered in this study). However, hydrogenative annihilation of all bulk defects in the 15 ML thick MgO films is unlikely, given the relatively large diffusion barrier for hydrogen in the MgO bulk lattice. (The experimental estimate for the diffusion coefficient of H^+ in Li-doped MgO is $1.2 \pm 0.4 \times 10^{-6}$ cm^2/s at $T = 1873$ K, while the diffusion activation energy is 1.9 ± 0.2 eV[33]. These values were obtained using infrared absorption measurements.)

2. Hierarchy of bulk defect stabilities

Potential candidates for causing the observed change in the photon emission spectrum are the F^{2+}-type defects within the defect complexes $2Li_{Mg}V_O$ and $(Li_{Mg}V_O)^+$ (orange lines in Fig. 6) and the F^+-type defects within $(2Li_{Mg}V_O)^-$ and $Li_{Mg}V_O$ (blue lines), since these defects exhibit an empty or half-filled defect level in the band gap.

Ball-and-stick models for all relevant defect configurations are shown in Fig. 7. Their relaxed coordinates and charge states are given in Table I. For defect complexes comprising an O vacancy there is an outward relaxation

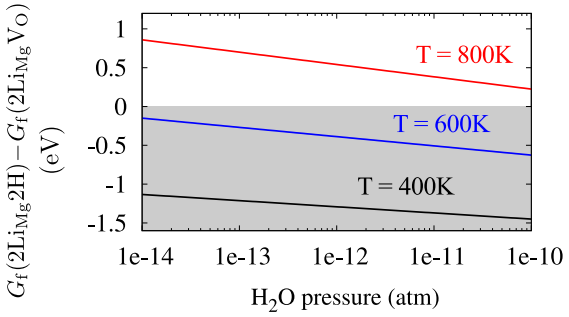

FIG. 5. Calculated free energy of hydrogenative annihilation of the $2Li_{Mg}V_O$ corner defect. The difference in free energy (calculated with HSE06) between the healed system (Fig. 4 (b)) and the system with a $2Li_{Mg}V_O$ defect complex (Fig. 4 (a)) is shown as a function of H_2O pressure for different temperatures. The $2Li_{Mg}V_O$ defect complex is thermodynamically unstable for temperatures and pressures, where the energy difference is negative (shaded in gray).

of nearest-neighbor Mg atoms and an inward relaxation of nearest-neighbor O atoms for F_s^{2+}-type and F_s^{+}-type O vacancies, while for F_s^{0}-type defects this trend is reversed and less pronounced.

Fig. 6 (a) shows the defect formation energies for the Fermi level at the VBM as a function of Li chemical potential. The Fermi level with respect to the VBM is denoted as $\Delta\epsilon_F$. In general, free formation energies of Li-containing defect configurations decrease and, consequently, their concentrations increase with increasing Li chemical potential. Within the whole range of Li chemical potential (from fully oxidized Li to a free Li atom), the hierarchy of formation energies for defect complexes comprising Li dopants and O vacancies can be classified in terms of the charge state of the included O vacancy, F^{2+}-type < F^{+}-type < F^{0}-type. In particular, the defect complexes with F^{+}- and F^{0}-type defects are so high in formation energy, that their calculated concentrations are negligible. For $\Delta\mu_{Li}$ close to Li in Li_2O and the Fermi level at the VBM, the order in formation energies for defect complexes comprising F^{2+}- and F^{+}-type defects is $(Li_{Mg}V_O)^{+} < 2Li_{Mg}V_O$ and $Li_{Mg}V_O < (2Li_{Mg}V_O)^{-}$, respectively. The lowest formation energy is $G_f((Li_{Mg}V_O)^{+})$=1.2 eV. Thus, $(Li_{Mg}V_O)^{+}$ will be the most abundant defect complex at an equilibrium temperature of 600 K and an O_2 pressure of 10^{-10} atm.

The order in formation energies for defect complexes comprising F^{2+}- and F^{+}-type defects is reversed within each charge state to $2Li_{Mg}V_O < (Li_{Mg}V_O)^{+}$ and $(2Li_{Mg}V_O)^{-} < Li_{Mg}V_O$, when the chemical potential of Li approaches the energy of a Li atom. Under these conditions, $Li_{Mg}Li_i$ is the defect complex with the lowest formation energy. For $\Delta\mu_{Li}$=3 eV and the Fermi level at the VBM, the thermodynamic stability of $Li_{Mg}Li_i$ is $G_f(Li_{Mg}Li_i)$=−3.1 eV. Among the defect complexes that comprise an oxygen vacancy, the $2Li_{Mg}V_O$ defect complex, which contains an F^{2+}-type defect, is thermodynamically most stable. For $\Delta\mu_{Li}$=3 eV and the Fermi level at the VBM, its formation energy is $G_f(2Li_{Mg}V_O)$=−2.6 eV. The situation where μ_{Li} equals the chemical potential of a Li atom corresponds to the sample being placed into an atmosphere of gaseous Li, a condition that is never fulfilled experimentally.

In Fig. 6 (b) the Fermi level is 1.5 eV above the VBM. Again, the formation energies for the different defect configurations are shown as a function of Li chemical potential. The general trend in formation energies of neutral defect complexes, F^{2+}-type < F^{+}-type < F^{0}-type in terms of the charge state of the O vacancy in the defect complex, is not affected by the shift in Fermi level. Only defect configurations carrying a net charge $q \neq 0$ depend on ϵ_F. The formation energy of the defect complex $(Li_{Mg}V_O)^{+}$, which contains an F^{2+}-type defect, is therefore shifted up by 1.5 eV, while the formation energy of $(2Li_{Mg}V_O)^{-}$, comprising an the F^{+}-type defect, is shifted down by 1.5 eV with respect to Fig. 6 (a), where ϵ_F=VBM. For $\Delta\mu_{Li}$=0 eV all defect complexes with O vacancy defects have formation energies higher than 2.5 eV. When Li is not fully oxidized, its chemical potential is raised and the defect complexes which contain F^{2+}-type defects can form more easily in thermodynamic equilibrium. However, at ϵ_F = 1.5 eV above the VBM, the defect complexes $(Li_{Mg}V_O)^{+}$ and $(2Li_{Mg}V_O)$, which comprise F^{2+}-type defects, have higher formation energies than Li_{Mg} and $Li_{Mg}Li_i$.

Fig. 6 (c) shows the dependence of the formation energies for the different defect configurations on the position of the Fermi level between VBM and conduction band minimum (CBm). The Li chemical potential is fixed at the value derived from the stability condition for Li_2O ($\Delta\mu_{Li}$=0 eV). The lowest transition levels between different defect configurations occur at ϵ_F=4.0 eV, when a $2Li_{Mg}V_O$ complex changes into $(2Li_{Mg}V_O)^{-}$, hence an F^{2+} defect is transformed into an F^{+} center. Correspondingly, the $(2Li_{Mg}V_O)^{-}$ becomes a $(2Li_{Mg}V_O)^{2-}$ complex (F^{+} to F^{0}-conversion) at an electron chemical potential of ϵ_F = 4.8 eV. Among the defects containing an O vacancy, the structural motif of two Li substitutional defects adjacent to one O vacancy is favored only when $\epsilon_F > 2.3$ eV, otherwise $(Li_{Mg}V_O)^{+}$ defects are easier to form. The main conclusion of Fig. 6 is that the most abundant bulk defect complexes that may cause the observed shift in the photon-emission peak are those comprising F^{2+}-type defects, namely $(Li_{Mg}V_O)^{+}$ and $2Li_{Mg}V_O$.

The theoretical analysis discussed above enables the following interpretation of the experimental data. For the given film thickness of 15 ML, the metal substrate below the film is an unsuitable electron source, as tunneling into MgO gap states is blocked by a substantial barrier. For the Li-doped films, this situation is best described by a Fermi level close to the VBM. For the Li chemical potential, as the second variable in Fig. 6, we consider lower μ_{Li} more realistic than higher values, as Li will be completely surrounded by O species from the MgO matrix after deposition/annealing. The most realistic situation is therefore displayed on the left side

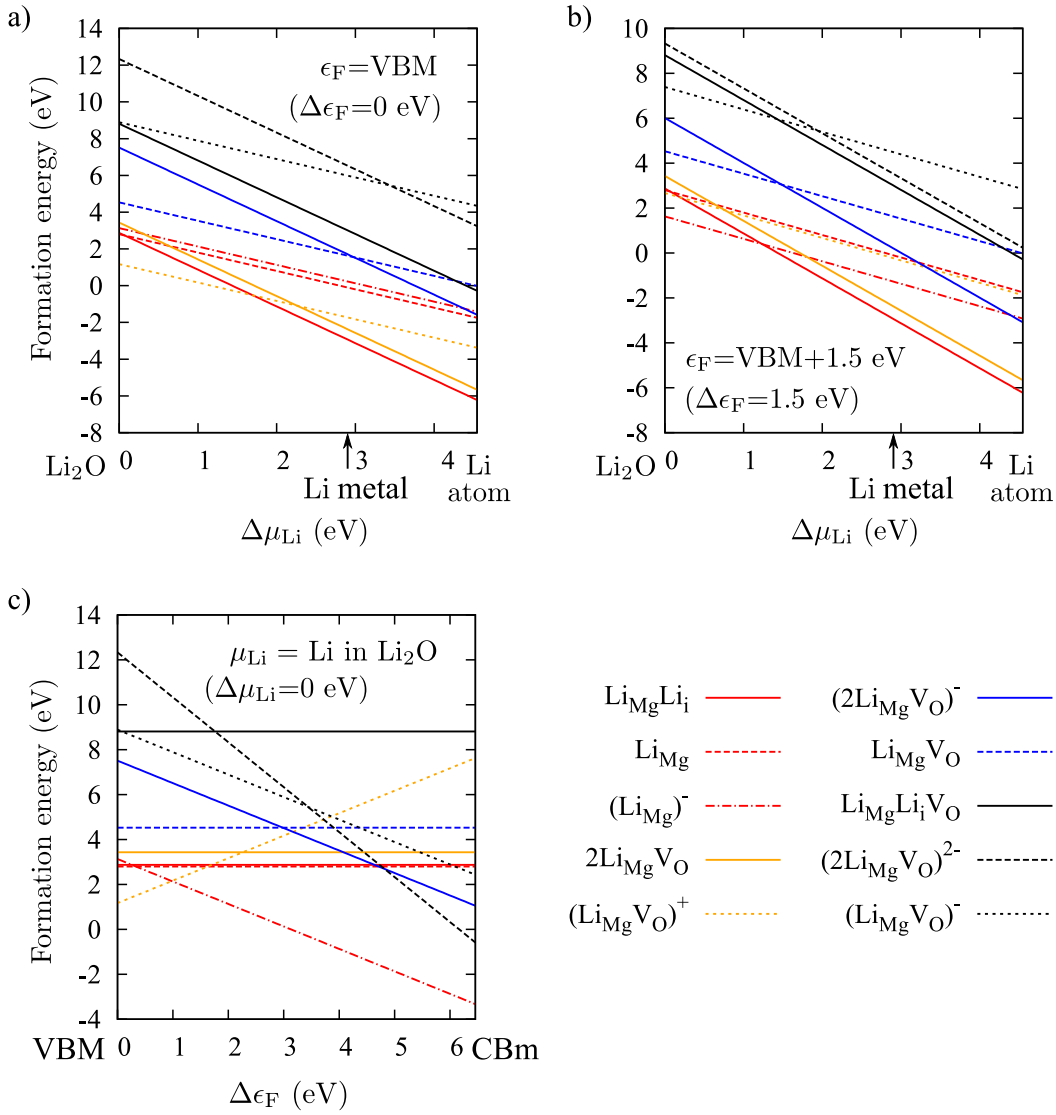

FIG. 6. Formation energies of different Li-mediated defect configurations at a temperature of 600 K and an O partial pressure of 10^{-10} atm. (a) and (b) show the formation energies as a function of the Li chemical potential, varied between the chemical potential of Li in Li_2O ($\Delta\mu_{Li}$=0 eV) and the chemical potential of a Li atom ($\Delta\mu_{Li}$=4.55 eV). The Fermi level is directly at the valence band maximum ($\Delta\varepsilon_F$=0 eV) in (a) and 1.5 eV above the VBM ($\Delta\varepsilon_F$=1.5 eV). In (c) the chemical potential of Li is $\Delta\mu_{Li}$=0 eV and the Fermi level is varied between VBM and conduction band minimum (CBm). Red lines show Li substitutional and interstitial defects without O vacancy, while all other defect configurations consist of one or two Li dopants adjacent to an O vacancy: Black lines show defect complexes comprising F^0-type defects, blue lines depict defect complexes including F^+-type defects, and orange lines represent defect complexes which contain F^{2+}-type defects.

of Fig. 6 (a,b, and c), respectively. Here, $(Li_{Mg}V_O)^+ < 2Li_{Mg}V_O < Li_{Mg}V_O$ is the predicted hierarchy of formation energies for defect complexes containing O vacancy defects and Li impurities. All the defects have characteristic defect states in the MgO band gap and can thus explain the shift in the optical spectra (see section III B 3). Note, that the Li defects without O vacancy are optically inactive and will therefore diminish the emission response when becoming the dominant species. The visibility of a red-shifted emission peak in Li-doped MgO therefore proves that the electronic/chemical conditions, at which Li_{Mg} and $Li_{Mg}Li_i$ defect complexes become energetically preferred, are not realized in the experiment (high Fermi levels, high Li chemical potentials). The electronic structure of the defect configurations, which comprise F^{2+} and F^+ defects, as the precondition for the optical response, will be discussed in the final section of this paper.

3. *Position of defect levels*

Our HSE06 calculations show that an unoccupied defect level is present deep in the band gap for the two defect complexes that contain F^{2+}-type defects, $(Li_{Mg}V_O)^+$

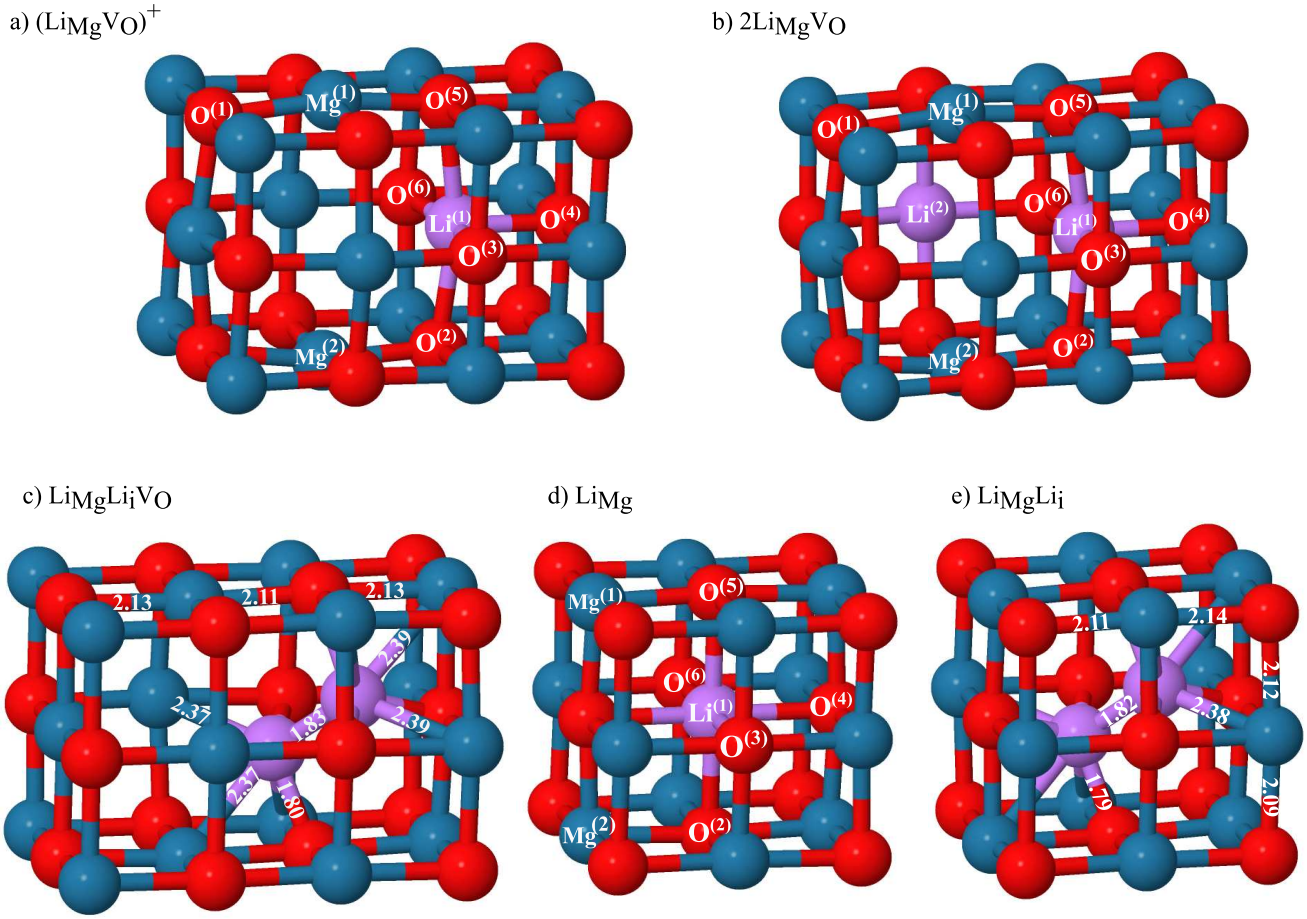

FIG. 7. Relaxed structures for (a) $(Li_{Mg}V_O)^+$, (b) $2Li_{Mg}V_O$, (c) $Li_{Mg}Li_iV_O$, (d) Li_{Mg}, and (e) $Li_{Mg}Li_i$. The shown structures have been cut out from the relaxed coordinates calculated using 216-atom supercells for neutral and 512-atom supercells for charged defect configurations. Relaxed coordinates not given here are listed in Table I.

and $2Li_{Mg}V_O$, opening a new channel for recombination of excitons created in the cathodo-luminescence experiment. The total and projected density of states (DOS) for the $(Li_{Mg}V_O)^+$ defect complex is shown in Fig. 8. The VBM is due to O 2 p states, while the defect level and the CBm are dominated by Mg 3 s states. The HSE06 Kohn-Sham defect-levels are at 4.2 eV for $(Li_{Mg}V_O)^+$ and at 4.4 eV for $2Li_{Mg}V_O$ with respect to VBM. For the defect complexes that comprise F^+-type defects the Kohn-Sham defect levels are 2.7 eV and 2.9 eV above the VBM for $Li_{Mg}V_O$ and $(2Li_{Mg}V_O)^-$, respectively. The overlap of different recombination channels involving different gap states might be responsible for the substantial peak broadening in emission spectra of Li-doped MgO.

Note, that a rigorous quantitative comparison between the position of the emission maximum in the cathodo-luminescence spectra and calculated defect level positions would involve employing an excited state theory, which is beyond the scope of this work.

For the changed optical response of Li-doped MgO compared to pure MgO, in principle two transitions come into consideration. De-excitation of a hot electron in the conduction band involves two steps, one from the CBm to the defect level and the second from the defect level to the VBM. Which transition is dominant for the photon emission depends on the symmetry of the contributing orbitals (Fig. 9). For both defect configurations, eigenstates at the CBm and in the defect have comparable symmetry, dominated by an s-shaped orbital arising from the Mg 3 s states. The state at the VBM, on the other hand, shows the distinct symmetry of the O 2 p states. The dipole selection rules for an optical transition can therefore only be fulfilled for the defect-level $\rightarrow$ VBM transition, where the state symmetry changes according to $\Delta l = \pm 1$, where l is the orbital momentum quantum number. The CBm $\rightarrow$ defect-level transition, in contrast, is dipole-forbidden, as the orbital symmetry remains constant. A comparison of spatial symmetries of the states therefore suggests, that the peak in the luminescence spectra is mainly due to transitions from the defect levels of defect complexes comprising F^+- and F^{2+}-type defects to the VBM.

TABLE I. Relaxed interatomic distances in Å for defect configurations in different charge states (compare Fig. 7). Corresponding distances are also given for pristine MgO for comparison. Distances between adjacent Li and O atoms $Li^{(i)}$-$O^{(j)}$, where Li has substituted a Mg atom in the lattice, can be compared to the distance between nearest neighbor Mg and O in pure MgO (2.11Å).

	pristine MgO	$2Li_{Mg}V_O$ F_s^{2+}-type	$(2Li_{Mg}V_O)^-$ F_s^{+}-type	$(2Li_{Mg}V_O)^{2-}$ F_s^{0}-type	$(Li_{Mg}V_O)^+$ F_s^{2+}-type	$Li_{Mg}V_O$ F_s^{+}-type	$(Li_{Mg}V_O)^-$ F_s^{0}-type	Li_{Mg} subst.	Li^-_{Mg} subst.
$O^{(1)}$-$Mg^{(1)}$	2.11	2.09	2.12	2.15	2.09	2.11	2.15	-	-
$Mg^{(1)}$-$Mg^{(2)}$	4.22	4.51	4.33	4.10	4.54	4.37	4.19	4.16	4.15
$O^{(1)}$-$O^{(2)}$	5.97	5.88	5.96	6.03	5.87	5.95	6.03	-	-
$Mg^{(1)}$-$O^{(5)}$	2.11	2.05	2.07	2.09	2.04	2.06	2.09	2.11	2.08
$Li^{(1)}$-$O^{(2)}$	-	2.15	2.15	2.16	2.14	2.15	2.16	2.16	2.17
$Li^{(1)}$-$O^{(3)}$	-	2.20	2.21	2.22	2.14	2.15	2.16	2.16	2.17
$Li^{(1)}$-$O^{(4)}$	-	1.90	1.99	2.09	1.89	1.98	2.07	2.16	2.17
$Li^{(1)}$-$O^{(5)}$	-	2.15	2.15	2.16	2.14	2.15	2.16	2.16	2.17
$Li^{(1)}$-$O^{(6)}$	-	2.09	2.10	2.11	2.14	2.15	2.16	2.16	2.17
$Li^{(2)}$-$O^{(6)}$	-	2.09	2.10	2.11	-	-	-	-	

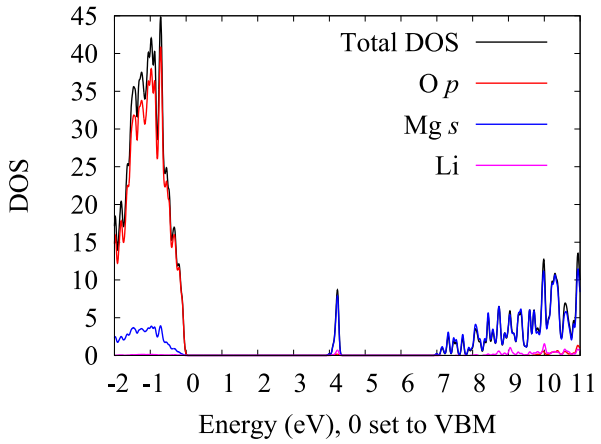

FIG. 8. Total and projected density of states for $(Li_{Mg}V_O)^+$ (the structure is shown in Fig. 7), comprising an F^{2+}-type defect, calculated with HSE06. The defect level is unoccupied. The size of the unit cell corresponds to the defect complex concentration of 3.1% (corresponding to 1 defect complex per 32 MgO units).

IV. CONCLUSIONS

The red-shift in the photon emission of Li-doped as compared to pristine MgO observed in STM luminescence spectra suggests the opening of new recombination channels for electron-hole pairs, being induced by defect-states in the oxide band gap. Whereas Li substitutional defects by themselves do not induce suitable gap states, defect complexes that consist of Li impurities and compensating O defects are likely candidates to generate the observed emission signature. While defect complexes containing electron-rich F^0-type O vacancies and Li dopants can be discarded in this context, as they are unstable, defect configurations comprising electron-poor F^+- and F^{2+}-type O vacancies that have lost electrons to the Li-induced hole states in the MgO valence band are compatible with the experimental results. From thermodynamic stability criteria established with DFT, defect complexes comprising doubly positively charged F^{2+} centers are most likely responsible for the red-shift of the emission peak to 550 nm, as they imprint a suitable defect state in the MgO band gap for electrons to decay from the conduction to the valence band. However, also defect complexes that contain F^+-type defects with a half-filled defect level are potential candidates. Given their higher formation energies with respect to different defect configurations that comprise F^{2+}-type O vacancies, we consider their contribution to the observed optical response of MgO_{Li} films as small.

Our combined experimental and theoretical study clearly demonstrates that the majority of Li dopants in MgO appears as defect complexes, comprising Li dopants and O defects, where local charge transfer between the O vacancy and one or two Li atoms annihilates the O 2 *p* hole states due to Li and therefore neutralizes the effect of the Li dopant. We hope that our results can help to improve understanding of the mechanisms of charge compensation in the bulk and thin-film oxide semiconductors in general, and in the doped MgO in particular.

V. ACKNOWLEDGEMENTS

This collaboration was financially supported by the cluster of excellence UniCat. N. A. R. acknowledges financial support from the International Max Planck Research School "Complex Surfaces in Materials Science". F. S. and S. V. L. acknowledge financial support from the Alexander von Humboldt-Foundation.

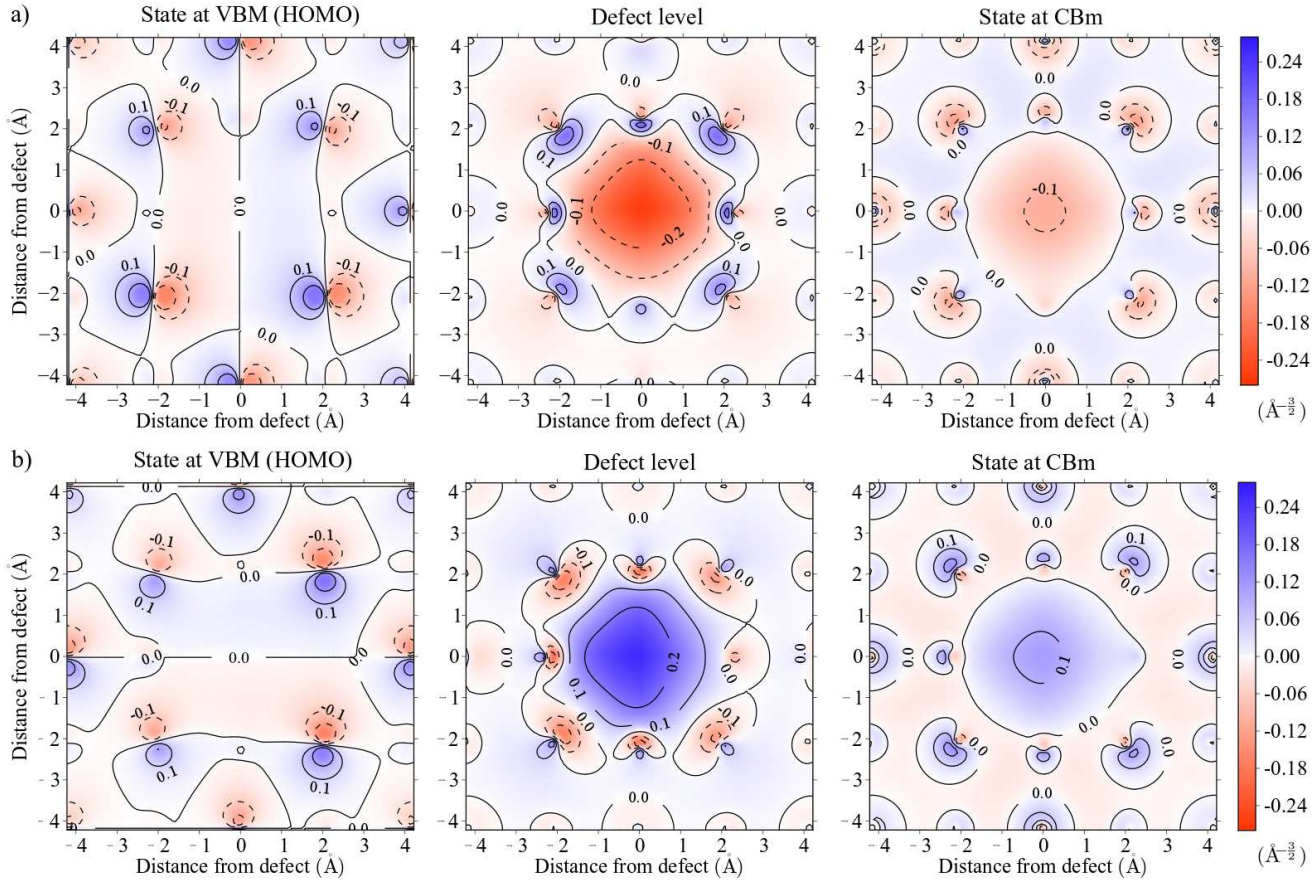

FIG. 9. Highest occupied valence state (*Left*), defect level (*Middle*), and lowest state in the conduction band (*Right*), in Å$^{-\frac{3}{2}}$, as a function of spatial coordinates in Å in the (100) plane for (a) $(Li_{Mg}V_O)^+$, where Li_{Mg} is at (0,-2.1) and V_O at (0,0) (see Fig. 7 (a) for comparison) and (b) $2Li_{Mg}V_O$, where **one** of the two Li_{Mg} is at (2.1,0) and V_O at (0,0) (see Fig. 7 (b) for comparison).

[1] T. Ito and J. H. Lunsford, Nature **314**, 721 (1985).
[2] P. Myrach, N. Nilius, S. Levchenko, A. Gonchar, T. Risse, K. Dinse, L. Boatner, W. Frandsen, R. Horn, H. Freund, R. Schlögl, and M. Scheffler, ChemCatChem **2**, 854 (2010).
[3] S. Arndt, G. Laugel, S. Levchenko, R. Horn, M. Baerns, M. Scheffler, R. Schlögl, and R. Schomäcker, Cat. Rev. **53**, 424 (2011).
[4] U. Zavyalova, M. Geske, R. Horn, G. Weinberg, W. Frandsen, M. Schuster, and R. Schlögl, ChemCatChem **3**, 949 (2011).
[5] C. Weinert and M. Scheffler, Mat. Sci. Forum **10-12**, 25 (1986).
[6] Y. Cui, S. Tosoni, W.-D. Schneider, G. Pacchioni, N. Nilius, and H.-J. Freund, Phys. Rev. Lett. **114**, 016804 (2015).
[7] J. Kramer, C. Tegenkamp, and H. Pfnür, Phys. Rev. B **67**, 235401 (2003).
[8] S. Benedetti, H. Benia, N. Nilius, S. Valeri, and H.-J. Freund, Chem. Phys. Lett. **430**, 330 (2006).
[9] S. Benedetti, P. Torelli, S. Valeri, H. M. Benia, N. Nilius, and G. Renaud, Phys. Rev. B **78**, 195411 (2008).
[10] D. Feller and K. A. Peterson, J. Chem. Phys. **110**, 8384 (1999).
[11] J. P. Perdew, K. Burke, and M. Ernzerhof, Phys. Rev. Lett. **77**, 3865 (1996).
[12] J. Heyd, G. E. Scuseria, and M. Ernzerhof, J. Chem. Phys. **118**, 8207 (2003).
[13] A. V. Krukau, O. A. Vydrov, A. F. Izmaylov, and G. E. Scuseria, J. Chem. Phys. **125**, 224106 (2006).
[14] N. A. Richter, S. Sicolo, S. V. Levchenko, J. Sauer, and M. Scheffler, Phys. Rev. Lett. **111**, 045502 (2013).
[15] A. Togo, F. Oba, and I. Tanaka, Phys. Rev. B **78**, 134106 (2008).
[16] V. Blum, R. Gehrke, F. Hanke, P. Havu, V. Havu, X. Ren, K. Reuter, and M. Scheffler, Comput. Phys. Commun. **180**, 2175 (2009).
[17] G. Makov and M. C. Payne, Phys. Rev. B **51**, 4014 (1995).
[18] C. Freysoldt, J. Neugebauer, and C. G. Van de Walle, Phys. Rev. Lett. **102**, 016402 (2009).
[19] C. W. M. Castleton, A. Höglund, and S. Mirbt, Phys. Rev. B **73**, 035215 (2006).
[20] D. K. Smith and H. R. Leider, J. Appl. Cryst. **1**, 246 (1968).
[21] A. Lichanot, C. Larrieu, R. Orlando, and R. Dovesi, J. Phys. Chem. Solids **59**, 7 (1998).

[22] M. M. Abraham, W. P. Unruh, and Y. Chen, Phys. Rev. B **10**, 3540 (1974).
[23] M. Abraham, Y. Chen, L. Boatner, and R. Reynolds, Phys. Rev. Lett. **37**, 849 (1976).
[24] J. A. Farmer, N. Ruzycki, J. F. Zhu, and C. T. Campbell, Phys. Rev. B **80**, 035418 (2009).
[25] L. Xu and G. Henkelman, Phys. Rev. B **82**, 115407 (2010).
[26] X. Shao, N. Nilius, and H.-J. Freund, J. Am. Chem. Soc. **134**, 2532 (2012).
[27] J. R. Jasperse, A. Kahan, J. N. Plendl, and S. S. Mitra, Phys. Rev. **146**, 526 (1966).
[28] S. Stankic, M. Müller, O. Diwald, M. Sterrer, E. Knözinger, and J. Bernardi, Angew. Chem. Int. Ed. **44**, 4917–4920 (2005).
[29] M. Anpo, Y. Yamada, Y. Kubokawa, S. Coluccia, A. Zecchina, and M. Che, J. Chem. Soc., Faraday Trans. 1: Physical Chemistry in Condensed Phases **84**, 751 (1988).
[30] A. L. Shluger, P. V. Sushko, and L. N. Kantorovich, Phys. Rev. B **59**, 2417 (1999).
[31] H. M. Benia, X. Lin, H.-J. Gao, N. Nilius, and H.-J. Freund, J. Phys. Chem. C **111**, 10528 (2007).
[32] M. Sterrer, M. Heyde, M. Novicki, N. Nilius, T. Risse, H.-P. Rust, G. Pacchioni, and H.-J. Freund, J. Phys. Chem. B **110**, 46 (2006).
[33] R. Gonzalez, Y. Chen, and K. L. Tsang, Phys. Rev. B **26**, 4637 (1982).